ELSEVIER

Journal of Crystal Growth 163 (1996) 329–338

JOURNAL OF CRYSTAL GROWTH

The case for a dynamic contact angle in containerless solidification

D.M. Anderson [a,1], M. Grae Worster [a,*], S.H. Davis [b]

[a] *Institute of Theoretical Geophysics, Department of Applied Mathematics and Theoretical Physics, University of Cambridge, Silver Street, Cambridge, CB3 9EW, UK*

[b] *Department of Engineering Sciences and Applied Mathematics, Northwestern University, Evanston, Illinois 60208, USA*

Received 22 December 1994; accepted 30 October 1995

Abstract

Containerless solidification, in which the melt is confined by its own surface tension, is an important technique by which very pure materials can be produced. The form of the solidified product is sensitive to conditions at the tri-junction between the solid, the melt and the surrounding vapor. An understanding of the dynamics of tri-junctions is therefore crucial to the modelling and prediction of containerless solidification systems. We consider experimentally and analytically the simple system of a liquid droplet solidifying on a cold plate. Our experimental results provide a simple test of tri-junction conditions which can be used in theoretical analyses of more complicated systems. A new dynamical boundary condition at the tri-junction is introduced here and explains the surprising features of solidified water droplets on a cold surface.

1. Introduction

Containerless solidification is one of the most common methods of growing crystals from melts. Many such systems (e.g. Czochralski crystal growth, float-zone processing, and laser welding) have complex geometries with free boundaries that are governed in part by the dynamics of the tri-junction, where the solid, its melt, and a vapor phase meet [1]. By influencing the shape of the liquid–vapor meniscus, the tri-junction can directly or indirectly (in conjunction with capillary- or buoyancy-driven convection) affect the crystal purity, uniformity and the presence of defects. An understanding of the dynamics of tri-junctions is therefore crucial to the modelling and prediction of containerless solidification systems. We explore four tri-junction conditions, each familiar in studies of evolving contact lines [2,3], in a simple model of the solidifying sessile water droplet (Fig. 1). The curious shape of the solidified water droplet provides a simple test of tri-junction conditions that can be used in theoretical analyses of more complicated systems. We discover that only by having a dynamic tri-junction condition can the observed inflexion in the shape of the solidified water droplet be predicted.

* Corresponding author. Fax: +44 1223 337918; E-mail: grae@esc.cam.ac.uk.

[1] Present address: Applied and Computational Mathematics Division, National Institute of Standards and Technology, Gaithersburg, Maryland 20899, USA.

0022-0248/96/$15.00 © 1996 Elsevier Science B.V. All rights reserved
SSDI 0022-0248(95)00970-1

2. Modelling

The geometry of our mathematical model follows those of previous authors [4–6] and is shown in Fig. 2. The solidifying droplet is axisymmetric with known initial contact angle ϕ_0 and volume v_0. We assume the solidification front to be planar. This is a simplifying assumption but one which is consistent with one-dimensional heat conduction through the solid. An apparent macroscopic contact angle ϕ defines the angle between the horizontal and the tangent to the liquid–vapor interface at the tri-junction.

The shape of the solidified droplet is determined by the evolution of the height of the solid–liquid interface h and the radial position of the tri-junction R. The evolution of the radius R, however, is coupled to the evolution of the volume v of the liquid portion of the droplet and the apparent contact angle ϕ. First, mass conservation relates the rate of change of liquid volume to the radius and solidification rate $\mathrm{d}h/\mathrm{d}t$ by

$$\frac{\mathrm{d}v}{\mathrm{d}t} = -\pi\rho R^2 \frac{\mathrm{d}h}{\mathrm{d}t}, \tag{2.1}$$

where $\rho = \rho_S/\rho_L$ is the density ratio (solid to liquid). Second, the shape of the liquid–vapor interface, which is a free boundary subject to the effects of capillarity and gravity, imposes a relation between R, v and ϕ. These two relations are sufficient to determine the shape of the solidified droplet once the contact angle is known. This angle is the focus of our study.

For simplicity and clarity we shall focus first on the case where gravitational effects are neglected. It is in this context where we first compare four different conditions imposed at the tri-junction. Once these conditions are introduced and analysed we shall then include the effects of gravity in the model in order to make more direct comparison with the experimental results.

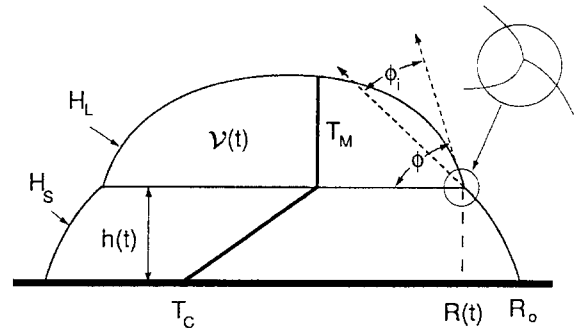

Fig. 2. A schematic diagram showing the features of the theoretical model used to describe how a droplet solidifies. The liquid–vapor interface is given by H_L, the solid–vapor interface by H_S, and the solid–liquid interface by h. The tri-junction is given by the intersection of H_L, H_S, and h. The radial coordinate of the tri-junction $R(t)$ evolves from the initial droplet radius R_0. It is the locus of the tri-junction that determines H_S, which, once formed, is constant in time. The growth angle ϕ_i is the angle between the tangents to the solid–vapor and liquid–vapor interfaces at the tri-junction. The liquid volume $v(t)$ decreases as the droplet solidifies. The inset shows the likely curvature of the solid–liquid interface very near the edge. A simplified tri-junction, with horizontal solid–liquid interface and an apparent contact angle ϕ is used in the models.

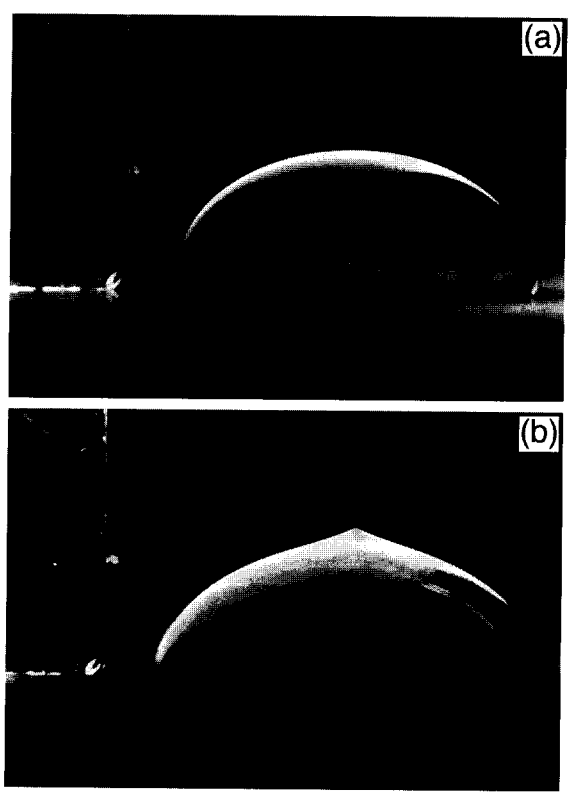

Fig. 1. (a) The initial water droplet at room temperature. The ruler on the left shows millimeter markings. The plate is cooled and freezes the droplet from below. The frozen droplet (b) has an inflexion point and a cusp-like apex.

2.1. Zero gravity

If the droplet is small (specifically, if the Bond number $B = \rho_L g l^2/\sigma$ is small, where ρ_L is the liquid density, g is the gravitational acceleration, l is the initial radius of the droplet, and σ is the liquid–vapor surface tension), then gravity can be neglected and surface tension holds the liquid–vapor interface in the shape of a spherical cap. Straightforward geometry relates the volume v of the liquid cap, the radius R of its base and the apparent contact angle ϕ via

$$v = \frac{2\pi R^3}{3} \frac{(1-\cos\phi)^2(1+\frac{1}{2}\cos\phi)}{\sin^3\phi}. \tag{2.2}$$

In what follows, we use Eqs. (2.1) and (2.2) and each of four different conditions at the tri-junction corresponding to fixed contact angle, fixed contact line, fixed growth angle and dynamic growth angle, to determine the shape of the solidified droplet.

2.1.1. Fixed contact angle

The simplest condition that one can impose is that the apparent contact angle remains at a fixed value, $\phi = \phi_0$. Here the liquid volume remains in the shape of a droplet in "static equilibrium" by slipping along the solid. The resulting solidified droplet is a straight-sided cone with profile given by

$$H_S(R) = \frac{3}{\pi R_0^2}\frac{v_0}{\rho}\left(1 - \frac{R}{R_0}\right), \tag{2.3}$$

where v_0 and R_0 are the initial droplet volume and radius, respectively, related via Eq. (2.2). The droplet evolution in this case is shown in Fig. 3. Note that the angle of the cone is not equal to ϕ_0. While this model illustrates that shape changes can occur during containerless solidification, it clearly does not describe the experimental observations.

2.1.2. Fixed contact line

An alternative, simple condition is obtained by keeping the contact line fixed and allowing ϕ to vary through a range of static contact angles [2,3]. The idea is that ϕ lies between a receding angle ϕ_R and an advancing angle ϕ_A but is otherwise not constrained. At each instant the tri-junction advances exactly in the direction of the liquid–vapor interface

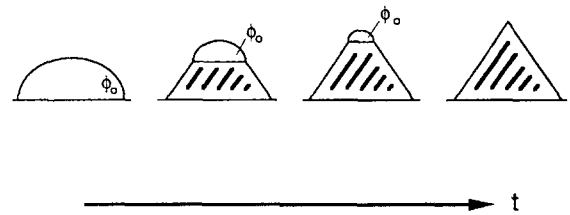

Fig. 3. Constant contact angle: four sketches of the droplet profile. The initial profile corresponds to an arc of a circle with contact angle ϕ_0. The solidification begins with a constant-sloped solid–vapor interface. The intermediate liquid–vapor interface is always circular with the same contact angle but at each instant in time encloses less volume. This evolution continues until the liquid volume vanishes, leaving a solidified droplet with a linear profile.

with no slipping, so that the contact line is essentially pinned. This tri-junction condition is written

$$\frac{dR}{dt} = -\frac{1}{\tan\phi}\frac{dh}{dt}. \tag{2.4}$$

The model is solved as described below and predicts that the solidified droplet is either concave upwards ($d^2R/dh^2 > 0$) or concave downwards ($d^2R/dh^2 < 0$), depending on the values of the initial contact angle ϕ_0 and the density ratio ρ relative to the dashed curve in Fig. 4. Note that while the droplet is three-dimensional (axisymmetric), the concavity of interest is that associated with the two-dimensional projection of the droplet surface so that the use of d^2R/dh^2 is appropriate. For an initial condition corresponding to a point below the dashed curve the droplets are concave up with nonzero slope at the top. For initial conditions above the dashed curve and with $\rho < 0.75$ the solidified droplets are concave down with nonzero slope at the top. For initial conditions with $\rho \geq 0.75$ the droplets are concave down with zero slope at the top. Therefore, a water droplet ($\rho = 0.917$) is predicted to solidify into a shape which is concave down with zero slope at its apex. Again this is inconsistent with the experimental observations.

2.1.3. Fixed growth angle

The previous condition is a special case (i.e. $\phi_i = 0$) of a more general condition in which the "growth angle" ϕ_i, defined as the angle between the tangents to the solid–vapor and liquid–vapor interfaces (Fig. 2), is held fixed [1,5,7,8]. The idea of a

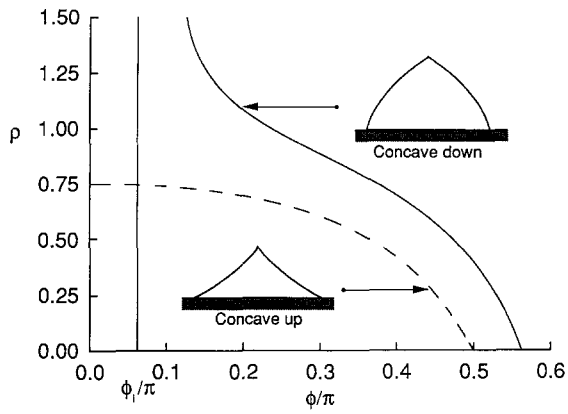

Fig. 4. Fixed contact line and fixed growth angle: A phase diagram of parameter values (ϕ,ρ) showing where the final profile is concave up or concave down when the growth angle ϕ_i is held fixed. When $\phi_i = 0$ and $\rho < 0.75$ the droplets are concave up for $\phi_0 < \phi_c(\rho)$ and concave down for $\phi_0 > \phi_c(\rho)$, where $\phi_c(\rho)$ is shown by the dashed curve. When $\phi_i = 0$ and $\rho \geq 0.75$, $\phi_c(\rho) = 0$, so all droplets are concave down and have zero slope at their apexes. In contrast, when $\phi_i \neq 0$ (the solid curve shows $\phi_i = 11°$), the tops of the solidified droplets are *always* pointed. Droplets with $\phi_i < \phi_0 < \phi_c(\rho)$ are concave up and droplets with $\phi_0 > \phi_c(\rho)$ are concave down, where $\phi_c(\rho)$ is shown by the solid curve. In all cases, the solidified droplet has final slope $-\tan(\phi_c(\rho) - \phi_i)$. Note also that $\phi < \phi_i$ is not physically possible. When $\phi_i = 0$ and $\rho = 1$, the final and initial shapes are identical. The evolution of the liquid angle ϕ at the tri-junction is from ϕ_0 at the base to $\phi_c(\rho)$ at the apex as indicated by the arrows. The insets show sketches of droplet profiles that are concave down (upper right) and concave up (lower left).

fixed growth angle was developed for containerless solidification by Bardsley et al. [9] and is based on arguments of local thermodynamic equilibrium. The actual value of this angle has typically been found experimentally [10,4]. Solutions in this case have been given by Sanz [5]. We present the main features in a somewhat simplified form here. Straightforward trigonometry shows that the tri-junction condition is expressed as

$$\frac{\mathrm{d}R}{\mathrm{d}t} = -\frac{1}{\tan(\phi - \phi_i)}\frac{\mathrm{d}h}{\mathrm{d}t}. \tag{2.5}$$

Eqs. (2.1) and (2.5) determine $\mathrm{d}v/\mathrm{d}h$ and $\mathrm{d}R/\mathrm{d}h$ respectively, and, together with Eq. (2.2), are solved numerically using a Runge–Kutta scheme to determine the final shape of the droplet.

For any fixed value of ϕ_i, the curvature of the solidified droplet $\mathrm{d}^2R/\mathrm{d}h^2$ is one-signed. The droplet is either concave up ($\mathrm{d}^2R/\mathrm{d}h^2 > 0$) or concave down ($\mathrm{d}^2R/\mathrm{d}h^2 < 0$) depending on whether ϕ_0 is less or greater than a critical angle $\phi_c(\rho,\phi_i)$ given implicitly by

$$\rho = 1 - \frac{(1-\cos\phi_c)^2}{\sin^4\phi_c}\left[1 + \left(2\cos\phi_c + \cos^2\phi_c\right) \times \left(1 - \frac{\tan\phi_c}{\tan(\phi_c - \phi_i)}\right)\right], \tag{2.6}$$

except when $\phi_i = 0$ and $\rho > 0.75$ in which case $\phi_c(\rho,\phi_i) = 0$. This expression corresponds to $\rho = a/f(a)$ in the notation used by Sanz [5], who identified this as the critical point of the system. The critical angle $\phi_c(\rho,\phi_i)$ is shown in Fig. 4 by the dashed curve for $\phi_i = 0$ (fixed contact line) and by the solid curve for a non-zero value of ϕ_i. As demonstrated by Sanz [5] and as indicated by the arrows in Fig. 4, $\phi \to \phi_c(\rho,\phi_i)$ as $R \to 0$ so Eq. (2.5) indicates that the slope $(\mathrm{d}h/\mathrm{d}R)$ at the apex of the solidified droplet is $-\tan[\phi_c(\rho,\phi_i) - \phi_i]$.

Previous investigators [4,5] have used this model to obtain estimates for ϕ_i for semi-conductor materials by fitting the theoretical droplet profiles to those obtained experimentally. Sanz et al. [6] extended this analysis to include the effects of gravity on the solidification of sessile and pendant droplets. This allowed for more accurate shape predictions on droplets of larger size. However, their theoretical predictions indicate that while gravitational effects can lead to an inflexion point in the case of pendant droplets, they do not lead to an inflexion point for sessile droplets. Therefore, none of the tri-junction conditions so far considered leads to a prediction of the observed change in concavity of the solidified water droplets.

2.1.4. Dynamic growth angle

The models using fixed contact angle or fixed non-zero growth angle inherently involve slipping at the tri-junction, which suggests that a dynamical condition on the contact angle may apply [2]. The idea of slipping at the tri-junction during containerless solidification has been suggested by Tropp and Yuferev [11], who noted the presence of a discontinuity in the velocity field at the tri-junction when $\phi_i \neq 0$, which can also be seen from the results of

Anderson and Davis [12]. That is, the fluid velocity at the tri-junction as measured along the liquid–vapor interface differs from the fluid velocity at the tri-junction as measured along the solidification front. The relation between slip and discontinuous velocity fields is perhaps more familiar in contact line problems involving the spreading of liquids along solid surfaces [13,2]. There, slip can be introduced at the moving contact line as a means of relieving the infinite force singularity created by the discontinuous velocity field. Note that slip in that context as well as in the present context is effective slip on a micron scale and not actual slip on a molecular scale. To understand the idea of slip further in the present context, recall first the case where $\phi_i = 0$. In this case, the direction of motion of the tri-junction is always locally tangent to the liquid–vapor interface and so there is no need to accommodate horizontal motion by slipping. In fact, if $\rho = 1$ in this case the initial and final droplet profiles are identical. When $\phi_i \neq 0$ or the fixed contact angle condition as described above is used, the direction of motion of the tri-junction is *not* aligned with the local tangent to the liquid–vapor interface. Our claim is that this additional motion should be related to slipping at the tri-junction. This horizontal slip velocity V_S is geometrically related to the solidification rate $V = \mathrm{d}h/\mathrm{d}t$ by

$$V_S = V\left(\frac{1}{\tan(\phi - \phi_i)} - \frac{1}{\tan\phi}\right), \tag{2.7}$$

(see Fig. 5) which can be inverted to give

$$\phi_i = \phi - \tan^{-1}\left[\left(\frac{V_S}{V} + \frac{1}{\tan\phi}\right)^{-1}\right]. \tag{2.8}$$

We note here that another possible geometric definition of the slip velocity involves slipping along the lateral solid surface (the solid–vapor interface) rather than along the horizontal solid surface (the solid–liquid interface) since in the present context these surfaces are not co-planar. If the slip velocity is defined to be along the lateral surface, a relation like that given in Eq. (2.7) is obtained for V_S but has "tan" replaced with "sin". We have analysed this possibility as well and have found no qualitative differences in the results. Therefore, in what follows, we shall assume that the horizontal slip velocity as

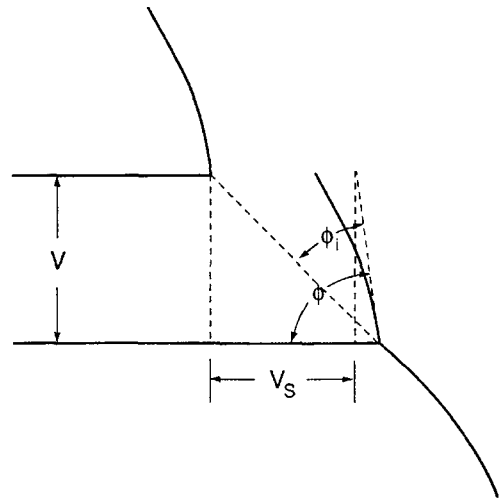

Fig. 5. Dynamic growth angle: a schematic diagram showing slipping motion of the tri-junction. When the solidification front advances at speed V and ϕ_i is nonzero, the contact line slips horizontally at a speed V_S. There is a geometrical relation between V, V_S, ϕ_i and the liquid angle ϕ given by Eq. (2.7). Note that the case $\phi_i = 0$ is consistent with no slip ($V_S = 0$).

defined by Eq. (2.7) is appropriate. We introduce a new condition at the tri-junction by assuming that there is a dynamical relation between this slip velocity V_S and the apparent contact angle ϕ. Here we use $V_S(\phi) = \eta(\phi_R - \phi)/\phi$ for $\phi < \phi_R$ and $V_S = 0$ for $\phi \geq \phi_R$, where ϕ_R is a receding angle and η is a characteristic slip velocity. Note that the dynamic growth angle condition is specified by this slip relation alone, since Eqs. (2.7) and (2.8) are geometrical identities. As is expected by the geometry of Fig. 2, we do not consider the possibility that the liquid drop spreads. We have investigated other forms of $V_S(\phi)$, such as $V_S(\phi) = \eta(\phi_R - \phi)^3$, and found little change in the results. The use of such spreading/receding relations has been well documented in the literature on the spreading of liquids on solids (see Refs. [2,3,14]) and it is our assumption that such a description applies in the present context. Note that with this dynamical condition ϕ_i is not constant; a fact that has been discovered experimentally [10,4] but has not previously been incorporated in theoretical analyses. In fact, direct measurements of digitized images of our experimentally solidified droplets also show that the growth angle ϕ_i is not constant. We shall discuss this further below.

The first three models (fixed contact angle, fixed contact line and fixed growth angle) are purely geometrical; the final shape is independent of the solidification rate. In contrast, with a dynamic growth angle, it is necessary to determine the rate of solidification in order to predict the solidified shape. By assuming one-dimensional heat conduction through the solid, and employing a quasi-steady approximation whereby the temperature field is taken to be linear, conservation of heat at the solid–liquid interface gives

$$h(t) = \left(2\frac{c\Delta T}{L}\kappa t\right)^{1/2}, \tag{2.9}$$

where c is the specific heat of the solid, L is the latent heat per unit mass, κ is the thermal diffusivity in the solid, and $\Delta T = T_M - T_C$, where T_M is the freezing temperature and T_C is the temperature of the cold plate.

We calculate the final droplet shape in the same way as in the previous model but the constant value of ϕ_i used in (2.5) is now replaced by its *dynamically determined* value given by (2.8). The solidification rate $V = dh/dt$ is initially infinite and decreases with time, giving (from Eq. (2.8) that ϕ_i is initially zero and increases once $\phi < \phi_R$. Thus, in the phase plane of Fig. 4, the separating curve $\phi_c(\rho, \phi_i)$ moves to the right as time evolves while the point representing the state of the system (with $\rho > 0.75$, say) moves to the left. Our calculations show that with a dynamic growth angle it is possible for the system to evolve from the concave-down region to the concave-up region to produce an inflexion point, as observed experimentally.

Before presenting these results graphically, we shall, with a qualitative basis for comparison established, incorporate the effects of gravity into the model to make possible more direct comparison with the experimental results.

2.2. Nonzero gravity and experiments

When the Bond number B is not small, the effects of gravity alter the shape of the solidified droplet indirectly through the direct effect on the shape of the liquid–vapor interface. In our experiments the Bond number is approximately 1.6 so gravity does play some role. The equation governing the shape of the liquid–vapor interface $H_L(r,t)$ is well known and is given here in dimensionless form by

$$B(H_L - h) - p = \frac{1}{r}\frac{\partial}{\partial r}\left(\frac{rH_{Lr}}{(1 + H_{Lr}^2)^{1/2}}\right) \tag{2.10}$$

where p is a spatially uniform pressure. The boundary conditions that apply are symmetry at $r = 0$ and $H_L = h$ and $\partial H/\partial r = -\tan\phi$ at the tri-junction $r = R$.

The solution to this equation must be found numerically and we follow the approach described by Huh and Reed [15], which was also used by Sanz et al. [6]. The solution of this equation gives the shape of the liquid–vapor interface and therefore relates the three variables R, v and ϕ. This relation then plays the role for nonzero B that Eq. (2.2) played for $B = 0$.

The system is closed by again using Eq. (2.1) and any one of the four tri-junction conditions discussed in the previous section. Since we have determined that only the dynamic growth angle model for the tri-junction leads to an inflexion point for zero gravity, we shall consider only that case below. Further, recall that the results of Sanz et al. [6] have shown that the inclusion of gravity for the case of constant ϕ_i does not lead to an inflexion point for sessile drops.

We conducted a series of experiments in which 35 μl droplets of distilled and de-aerated water were frozen from below on a cold aluminum plate for a range of plate temperatures. Care was taken to assure consistency in the initial conditions of the droplets. The droplet diameters were kept consistent by placing each droplet on a raised disk of diameter 7 mm and a micropipette was used to place drops of consistent volume. The water droplets froze from below as a nearly planar solidification front advanced upwards through the droplet. A typical freezing time with $\Delta T = 10°C$ was 40 s. We believe that as a consequence of this rapid growth, we are above the roughening transition in the experiments and are dealing with continuous rather than facetted growth. Typical profiles before and after solidification are shown in the photographs in Fig. 1. As pointed out previously, the solidified droplet profile has an identifiable inflexion point. Video images of the frozen droplets

were digitized in order to allow direct comparison with theoretically predicted shapes. Fig. 6 shows typical initial and resulting final profiles obtained experimentally (open circles and open diamonds, respectively). These data correspond to a droplet solidified with undercooling $\Delta T = 10°C$ and measured inflexion point near $R/R_0 = 0.21$ (see below and Fig. 7). To compare our theoretical results to the experimental results we first obtained the appropriate values of R_0, v_0 and ϕ_0 to fit the initial profile. We find good agreement between the theory (lower solid curve) and experiment for the initial droplet shape. With these initial conditions we then chose the parameters ϕ_R and η to "best fit" the experimentally solidified droplet profile. The result for $\phi_R = 0.12\pi$ and $\eta = 0.6$ mm s^{-1} (upper solid curve) indicates that the theoretically calculated profile agrees quite well with the experimentally obtained profile. For further comparison, the solidified shape predicted for a fixed growth angle of $\phi_i = 0$ (gravity included) is shown by the dashed curve. While it is not clear exactly how to vary the two free parameters ϕ_R and η to get the best fit, we are guided by the fact that

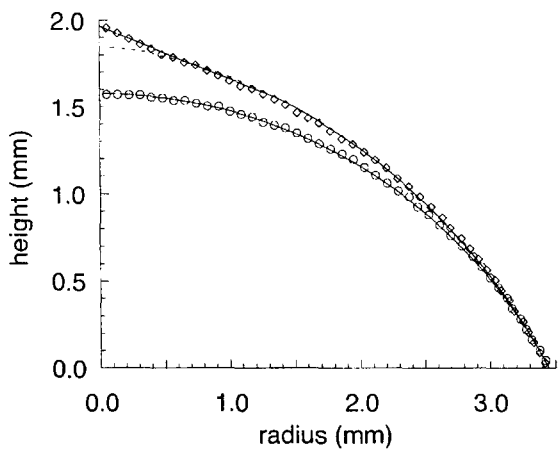

Fig. 6. Experimental initial and final profiles compared with those computed theoretically. The open circles represent the initial droplet profile measured experimentally and the open diamonds represent the resulting experimentally solidified droplet ($\Delta T = 10°C$). With the initial values of $v_0 = 33.05$ and $R_0 = 3.45$ chosen so that the initial droplet profile computed theoretically (lower solid curve) fit the experimental initial profile, we chose the values of ϕ_R and η to best fit the experimentally solidified droplet profile. The upper solid curve shows the theoretical prediction for $\phi_R = 0.12\pi$ and $\eta = 0.6$ mm s^{-1}. The material parameters were taken to be $B = 1.6$ and $\rho = 0.917$. For comparison purposes we have shown the predicted solidified shape when the growth angle ϕ_i is taken to be zero (dashed curve).

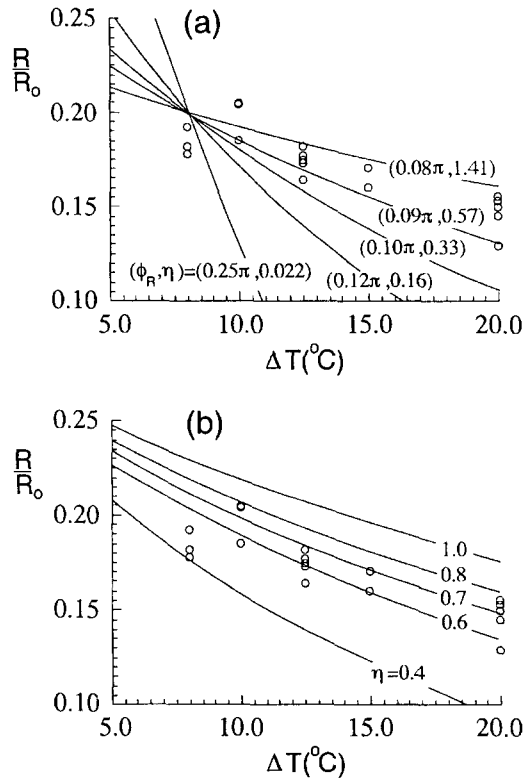

Fig. 7. Experimental data (open circles) and theoretical predictions (solid curves) of the radial coordinate R of the inflexion point in the solidified droplets for different parameter values ϕ_R and η. The experimental data was obtained through a series of experiments in which 35 μl droplets of distilled and de-aerated water were frozen from below on a cold aluminum plate for a range of plate temperatures. Video images of the frozen droplets were digitized and a local curve-fitting procedure was used to determine the position of the inflexion point. The scatter in the data is representative of the error involved in determining the precise location of the inflexion point from the digitized images. The theoretical results were obtained using the slip law $f(\phi) = \eta(\phi_R - \phi)/\phi$. In (a), ϕ_R is varied and η (given in units of mm s^{-1}) is chosen so that the curves pass through a common point. This figure shows that a value of $\phi_R = 0.09\pi \pm 0.01\pi$ ($16° \pm 2°$) is required to predict the observed rate of variation of R with undercooling ΔT. Figure (b) has $\phi_R = 0.09\pi$ and shows that a value of $\eta = 0.6 \pm 0.2$ mm s^{-1} provides a reasonable fit of the experimental data. These empirical values are approximate to the extent that the model used to determine them incorporates a number of simplifying assumptions and the data used to fit them contains a fair amount of scatter.

the value of ϕ_R effectively determines the point at which the droplet shape deviates from that predicted with $\phi_i = 0$ (the solid and dashed curves coincide until ϕ_i becomes nonzero in the dynamic growth angle calculations) and η measures the strength of this deviation. Note that while the case with $\phi_i = 0$ fits the lower part of the solidified droplet well, it differs noticeably near the top. We note here the difficulty in identifying a precise location of the inflexion point from the digitized image.

As was the case for zero gravity, we find that the using of the dynamic growth angle condition here predicts that it is possible for the solidified droplet to have an inflexion point. Further, we find that the predicted shape of the solidified droplet varies with the solidification rate. In particular, the radial coordinate of the inflexion point is predicted to decrease with increasing undercooling ΔT. To test this prediction, a local curve-fitting procedure was used to determine the position of the inflexion point from the digitized images of droplets solidified at different undercoolings. We find that for our experimentally solidified droplets the radial coordinate of the inflexion point decreases with increasing undercooling ΔT (see open circles in Fig. 7). The scatter in the data is representative of the error involved in determining the precise location of the inflexion point from the digitized images. These experimental results agree qualitatively with the theoretical trends predicted by direct calculation of the solidified droplet profiles, as shown in Fig. 7 by the solid curves corresponding to different values of ϕ_R and η. The theoretical results were obtained using the slip relation $f(\phi) = \eta(\phi_R - \phi)/\phi$. In Fig. 7a, ϕ_R is varied and η (given in units of mm s^{-1}) is chosen so that the curves pass through a common point. This figure indicates that a value of $\phi_R = 0.09\pi \pm 0.01\pi$ required to predict the observed rate of variation of R with undercooling ΔT. Fig. 7b has $\phi_R = 0.09\pi$ (16°) and shows that a value of $\eta = 0.6 \pm 0.2$ mm s^{-1} leads to a reasonable fit of the experimental data.These empirical values are approximate to the extent that the model used to determine them incorporates a number of simplifying assumptions and the experimental data used to fit them contains a fair amount of scatter. Nonetheless, we expect that the overall trend indicating that the position of the inflexion point moves towards the center of the droplet as the undercooling is increased, which is predicted theoretically and observed experimentally, is robust. An important overall idea, which is quantified in Fig. 7, is that the shape of the solidified droplet varies with solidification rate.

We note that the best fit values of η and ϕ_R based on the position of the inflexion point (Fig. 7b) differ from the best fit values based on the overall shape (Fig. 6), which predict an inflexion point near $R/R_0 = 0.3$. That is, the values predicted in Fig. 7 fit the overall trend but do not necessarily fit any one particular experiment. However, the dynamic growth angle model appears to capture the same behavior in terms of the dependence of the inflexion point position on the undercooling and is also able to fit the experimental profiles reasonably accurately.

Finally, we have calculated the variation in ϕ_i directly from the digitized images and compared the results with the theoretical predictions. In order to calculate ϕ_i from images of the initial and final solidified shape alone, we need to predict theoretically the liquid–vapor interface shape at intermediate stages. The results of Fig. 6 demonstrate that this can be done accurately. For any given height h we measure the radius and solid slope (or equivalently the solid angle ϕ_S) directly and compute the solid volume $v_S(h)$ numerically. Next, the liquid volume $v_L(h)$ for any height h can be computed from the solid volume at that height and the initial and final volumes, v_0 and v_f, respectively, using the relation $v_L(h) = v_0 - (v_0/v_f)v_S(h)$. Then, given the liquid volume and radius, the shape of the liquid–vapor interface is computed theoretically and the liquid angle ϕ is obtained. The growth angle at any height is given by $\phi_i = \phi - \phi_S$. Fig. 8 shows these results for the same experimental droplet as shown in Fig. 6. For comparison purposes, we show two sets of data corresponding to the cases where the liquid–vapor interface, as described above, is computed with $B = 0$ (lower data points) and $B = 1.6$ (upper data points). This comparison illustrates the expected result that the effects of gravity increase ϕ and therefore ϕ_i. Also shown by the solid curve is the predicted variation of ϕ_i with h corresponding to the best fit profile in Fig. 6. While the fit between theory and experiment is not perfect (the appropriate comparison is with the upper set of data), both results are dominated by small or zero growth angle for the lower portion of the droplet and increased growth

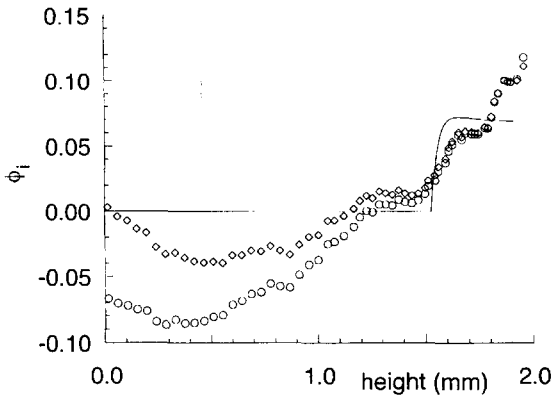

Fig. 8. Experimental data showing the variation in growth angle ϕ_i with height h. The experimentally measured variation of ϕ_i is shown by the open diamonds (with the liquid–vapor interface calculated with $B = 1.6$) and by the open circles (with the liquid–vapor interface calculated with $B = 0$). The error in the measured value of ϕ_i can be estimated to be ± 0.02. The solid curve represents the value of ϕ_i from the theoretical results using the dynamic growth angle condition (and corresponding to the theoretically calculated profile in Fig. 6).

angle near the top. The error involved in measuring ϕ_i from the digitized image data can be estimated to be ± 0.02 and is one possible explanation for the measured negative growth angles during the initial stages of growth.

The results shown in Fig. 8 indicate quite clearly that the growth angle ϕ_i in our experiments is not constant and suggest that our growth rates are too fast to allow relaxation to equilibrium tri-junction conditions, which would predict a constant value of ϕ_i[9]. While it is possible, for example, that the nature of crystallisation changes from the bottom of the droplet to the top (perhaps polycrystalline near the bottom with $\phi_i = 0$ to monocrystalline near the top with $\phi_i \neq 0$), this issue is difficult to resolve given the level of sophistication of our experiments. Further, since we have treated the tri-junction by using overall balances, the model neglects microscopic details associated with the poly/monocrystalline nature of solidification in favour of a macroscopic description. We additionally note that the symmetry of the solidified droplets and the lack of flat facets on the solidified droplet surface suggest that we are dealing here with continuous rather than facetted growth. In any case, it seems apparent that when solidification occurs at a tri-junction where the growth angle is nonzero, there must accompany a slipping of the liquid on the solid. The simple model for the solidification of a water droplet in conjunction with our proposed dynamic growth angle condition appears to support this claim.

3. Summary

We have investigated theoretically and experimentally the simple configuration of a liquid droplet solidifying on a cold plate. We find that the experimentally solidified water droplet has an inflexion point and a cusp-like top. Further, the position of the inflexion point varies with the solidification rate. We considered a simple theoretical model (both with and without gravitational effects) in which four different tri-junction boundary conditions could be tested. These conditions correspond to fixed contact angle, fixed contact line, fixed growth angle [5], and dynamic growth angle. We find that only with a dynamic growth angle can an inflexion point in the solidified droplet profile be predicted. Both theory and experiment predict that the radial coordinate of the inflexion point decreases with increasing undercooling. We have shown that it is possible to obtain reasonable fits to the experimentally solidified droplet profiles. Further, analysis of our experimental data indicates that the growth angle ϕ_i is not constant throughout the solidification process. Our theoretical predictions agree qualitatively with this result.

Several critical issues in containerless solidification hinge upon an accurate description of the tri-junction. The shape of the free melt–vapor interface can influence various forms of buoyancy- and capillary-driven flows of the melt. These flows alter the distribution of heat and solute in the melt, and hence are crucial in determining the resulting composition and structure of the solid. In order to predict the shape of the free interface, accurate conditions at the tri-junction are needed. Also, the premature detaching of the crystal from the melt during Czochralski growth, for example, is a dynamic event controlled directly by wetting effects at the tri-junction. The present study indicates that in order to address these issues, a dynamic tri-junction condition that takes

into account the slipping of the contact line is required. We hope that our introduction of this idea will stimulate others capable of performing more sophisticated experiments to investigate this hypothesis more fully.

Acknowledgements

This work was supported by grants from the National Aeronautics and Space Administration through the Microgravity Science and Applications Division and from the Natural Environment Research Council. We are grateful to M. Elliott for assistance with the experiments, S. Dalziel for access to DigImage, used to gain profiles of the droplets, and to H.E. Huppert and B.J. Spencer for helpful comments on an earlier draft of this paper. We also wish to thank the referees for bringing to our attention a number of issues related to the nature of crystallisation.

References

[1] R.A. Brown, AIChE J. 34 (1988) 881.
[2] E.B. Dussan V, Ann. Rev. Fluid Mech. 11 (1979) 371.
[3] P.G. de Gennes, Rev. Mod. Phys. 57 (1985) 827.
[4] G.A. Satunkin, V.A. Tatarchenko and V.I. Shaitanov, J. Crystal Growth 50 (1980) 133.
[5] A. Sanz, J. Crystal Growth 74 (1986) 642.
[6] A. Sanz, J. Meseguer and L. Mayo, J. Crystal Growth 82 (1987) 81.
[7] J.L. Duranceau and R.A. Brown, J. Crystal Growth 75 (1986) 367.
[8] G.W. Young and A. Chait, J. Crystal Growth 96 (1989) 65.
[9] W. Bardsley, F.C. Frank, G.W. Green and D.T.J. Hurle, J. Crystal Growth 23 (1974) 341.
[10] T. Surek and B. Chalmers, J. Crystal Growth 29 (1975) 1.
[11] E.A. Tropp and V.S. Yuferev, Izv. Akad. Nauk SSSR, Ser. Fiz. 47 (1983) 274 [English translation: Bull. Acad. Sci. USSR, Phys. Ser. 47 (1983) 63].
[12] D.M. Anderson and S.H. Davis, J. Crystal Growth 142 (1994) 245.
[13] E.B. Dussan V. and S.H. Davis, J. Fluid Mech. 65 (1974) 71.
[14] P. Ehrhard, J. Fluid Mech. 257 (1993) 463.
[15] C. Huh and R.L. Reed, J. Colloid Interface Sci. 91 (1983) 472.